

Weldeyohannes, T. T., Hailu, B. T., Muluneh, A. A., Kidane, T. (2022): Detection of geothermal anomalies in the Northern Lake Abaya geothermal field, Main Ethiopian Rift. - Journal of Volcanology and Geothermal Research, 430, 107638.

<https://doi.org/10.1016/j.jvolgeores.2022.107638>

**Detection of geothermal anomalies in the Northern Lake Abaya geothermal field, Main Ethiopian Rift**

Tsion Taye Weldeyohannes<sup>1,\*</sup>, Binyam Tesfaw Hailu<sup>1,2</sup>, Ameha Atnafu Muluneh<sup>1,3</sup>, Tesfaye Kidane<sup>4</sup>

<sup>1</sup>School of Earth Sciences, Addis Ababa University, Addis Ababa, Ethiopia.

<sup>2</sup>Departments of Geosciences and Geography, University of Helsinki, Finland.

<sup>3</sup>Helmholtz-centre Potsdam - GFZ German Research Centre for Geosciences, Potsdam, Germany.

<sup>4</sup>School of Agricultural, Earth and Environmental Sciences, UKZN, Westville, Durban, 4001, South Africa

**\*Corresponding author:** Tsion Taye Weldeyohannes: 23tsiontaye@gmail.com

## ABSTRACT

The detection of geothermal anomalies using Thermal Infrared (TIR) remote sensing data is challenging because of how sensor specifications (such as the infrared wavelength used for the measurement, spectral dependence of the emissivity, angle at which the measurement is made, state of the surface and height of the sensor above the surface) and physical parameters (such as solar radiation, topography, albedo, soil compaction and coherence of rocks) affect Land Surface Temperature (LST) retrieval and analysis. This work tests whether TIR remote sensing measurements with thorough spatial and temporal sampling can improve LST retrievals. Multi-temporal TIR data from 2000 through 2019 from Landsat 7 and 8 TIR instruments and the Advanced Spaceborne Thermal Emission and Reflection Radiometer (ASTER) were used to detect geothermal areas in the geologically active region of the southern Main Ethiopian Rift. In addition, field-based temperature data from 19 sites were evaluated for comparison to the remotely detected geothermal anomaly areas. We have used the single channel algorithm and Normalized Difference Vegetation Index (NDVI) method of emissivity retrieval to derive LST for each year. The result shows that the mean LST is highest in 2003 (320.1 K) and lowest in 2019 (303.1 K). The change in mean LST was between -9 K to 13 K. These LST results from ASTER images were validated with MODIS LST products and showed a correlation coefficient greater than 0.6. LST of the year 2003 has been much closer to the actual temperature value from field data. Fifteen sites (79 %) fit with the identified geothermal anomaly areas. LST values in known geothermal activity sites show no correlation (< 0.5) with time attesting. That is, even though LST varies with time (e.g., day and night and seasonal changes), the LST of areas with geothermal potential remain more or less constant on yearly basis.

**Key Words:** Land Surface Temperature (LST), Geothermal Anomaly, Main Ethiopian Rift (MER), Thermal Infrared (TIR).

## 1. INTRODUCTION

Geothermal energy is the energy of the ‘Earth’s Heat’ and is an essential backbone for the world’s sustainable energy source and an important component of green energy in the globe. The renewability and environmental friendly nature along with multipurpose applications makes geothermal energy one of the most favored energy sources in the modern age (Chan et al., 2018, Muhammed, 2019).

The East African Rift System (EARS) is an active volcano-tectonic region where heat energy from the Earth’s interior escapes to the surface in the form of volcanic eruptions and geothermal surface manifestations. The presence of high enthalpy geothermal system (usually defined as a geothermal system characterized by reservoir temperature above 150–225°C (e.g., Reinsch et al., 2017) shows the existence of shallow heat sources, groundwater, and intense faulting in the rift (e.g., Abiye, 2003; Teklemariam, 2008; Omenda and Teklemariam, 2010; Pürschel, 2013).

Despite the vast geothermal potential in the EARS, a detailed survey is limited to few sites in the rift due to huge exploration cost (e.g., Pürschel et al., 2013; Minissale et al., 2017). Remote Sensing is a viable tool for geothermal resource exploration since it minimizes the ground-based surveys’ cost and effort. It can also give valuable information such as surface temperature anomalies and structural control of the Earth surfaces that could lead to the findings of geothermal surface expressions and ultimately to locate new geothermal prospect areas (e.g., Van der Mee et al., 2014). In recent studies, the launch of spaceborne platforms such as Landsat satellites, Advanced Spaceborne Thermal Emission and Reflection Radiometer (ASTER) and the Moderate Resolution Imaging Spectroradiometer (MODIS) have drastically improved data quality and availability; which resulted in an increase in geothermal exploration and detection studies using remote sensing (e.g. Eneva et al., 2006; Coolbaugh, et al., 2007; Qin, et al., 2011; Vaughan, et al., 2012; Haselwimmer, et al., 2013; Calvin et al., 2015; Chan et al., 2018; Darge et al., 2019).

Land Surface Temperature (LST) anomaly is a key indicator of geothermal areas in TIR remotely sensed imagery. It can give an insight to locations of surface heat manifestations with geothermal energy potential. Areas with larger LST values than the background are considered to be anomalous.

Recently, Darge et al., 2019 used Landsat image analysis to detect geothermal anomalies in Tulu Moye geothermal prospect, Main Ethiopian Rift (MER). Although a one-time satellite image analysis can be used to identify promising geothermal sites (e.g., Qin et al., 2011; Darge et al., 2019; Wang et al., 2019), a multi-temporal image analysis could give a better result. This is because a multi-temporal analysis will help in the elimination of false anomalies (both false positives and false negatives) and could provide a better result. This means if an analyst identifies one place as a geothermal anomaly area in a year  $x$ , that place should be anomalous consistently throughout the given time frame to be verified as geothermal sites. Otherwise, the estimated anomaly might be a false one resulting from other factors. Moreover, a multi-temporal analysis will also give a privilege to map and monitor changes (if any) observed on the surface heat manifestations (e.g., Braddock et al., 2017; Darge et al., 2019).

Ethiopia hosts several high–enthalpy geothermal sites, mainly in the Ethiopian and Afar rifts. However, detailed exploration is limited to Aluto-Langano, Corbetti and Tendaho sites. In the present study, we used multi-temporal satellite image analysis from the year 2000 onwards (in two years intervals except for some cases) on Lake Abaya geothermal prospect using multi-sensor thermal remote sensing data to detect anomalous areas and evaluate LST. The results are then compared with borehole data compiled

from different kinds of literature. Our study improves exploration strategies in regions where direct exploration may not always be feasible.

## 2. Geology and Hydrothermal activity of Abaya.

The Main Ethiopian Rift forms an active tectonic boundary between Nubia and Somalia plates and is characterized by along axis variation in volcanism and deformation (e.g., Muluneh et al., 2017). In the southern MER deformation is accommodated on the rift bounding faults, whereas, in the northern MER, it is mainly localized at the rift floor faults, known as Wonji Fault Belt (e.g., Keir et al., 2006, Corti et al., 2020). In the central MER, both faults belonging to the Wonji Fault Belt and border faults are active (Corti et al., 2020; Agostini et al., 2011). In general, the MER is dominated by transtensional deformation (e.g., Muluneh et al., 2014). Siegburg et al., 2020 showed that the transtensional deformation is more significant in the northern MER than the central and southern MER. Seismicity study around many of the volcanoes in the MER shows that earthquakes are clustered on faults that are assumed to channel hydrothermal fluids (Greenfield et al., 2020; Lapins et al., 2020; Muluneh et al., 2021).

The present study area, which includes the Abaya geothermal project, is dominated by a series of normal faults oriented in NE-SW directions (e.g., Minissale et al., 2017). These faults allow fluids to migrate to a shallower depth and are also associated with seismicity (Ogden et al., 2021). The study area has a series of normal faults and is characterized by an elevation between 2251 and 1161 m a.s.l.

The geology of the area includes rock types such as obsidians, basalt flows, pumiceous pyroclastics, ignimbrites, and lake sediments (Chernet.2011). The rift floor is dominated by flat volcano-sedimentary plains with an average elevation of 1300 m a.s.l and is characterized by a series of sub-parallel normal faults and NNE-SSW trend forming horsts and graben structures. The study area is part of a closed drainage system within the southern MER, with all rivers and streams draining into Lake Abaya.

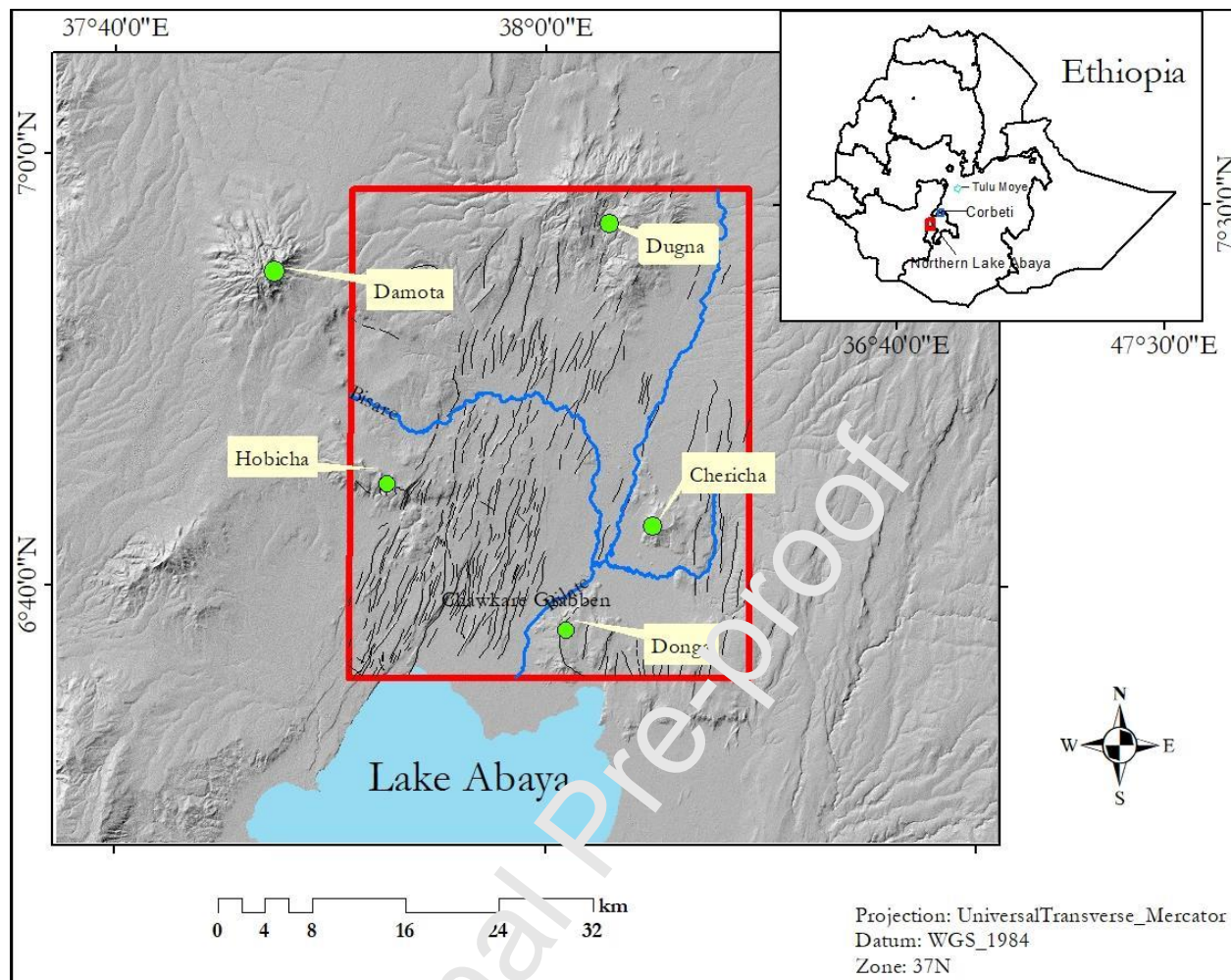


*Figure 1.* Location map of the study area in the southern MER. Green dots are Pleistocene and Holocene volcanoes. Black lines are faults from Chernet (2011). The open red square shows the extent of the geologic map shown in Figure 2.

The central and northern part of the study area is drained by Bilate River and its tributaries such as Bisare and Derba, which form a delta at its confluence into the north shore of Lake Abaya (e.g., Chernet, 2011). (Fig 1).

A variety of active hydrothermal manifestations are found in the Abaya area. Most hydrothermal features are concentrated along with the NNE-SSW trending fault system on the western part of the Chewkare graben. The main hydrothermal manifestations are fumaroles, thermal springs, hot springs, bubbling and boiling pools. Spring temperatures are as high as 96°C with a high flow rate (e.g., Ayele et al., 2002; Chernet, 2011). (Fig 2)

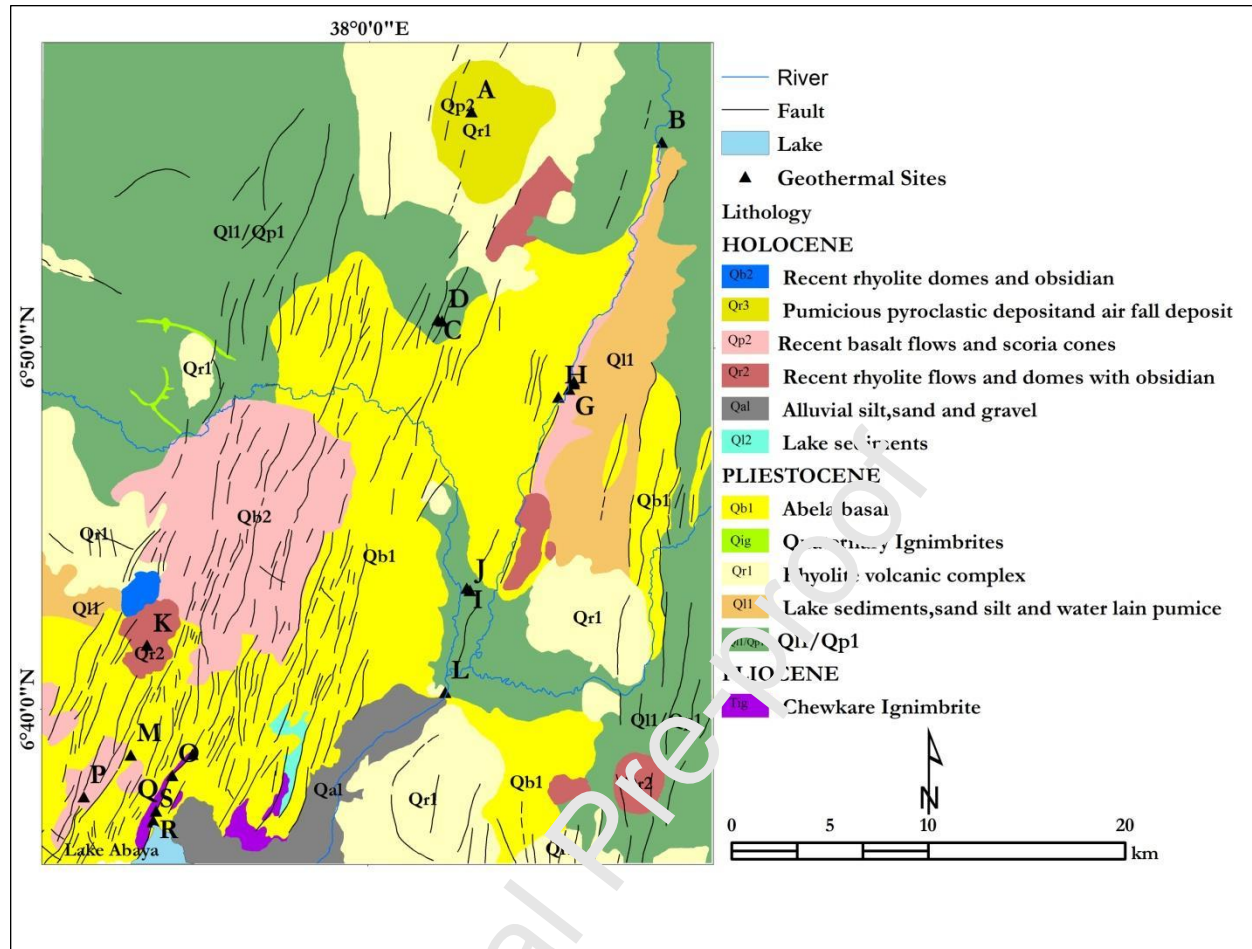


Figure 2. Geological map and known geothermal sites near the Northern Lake Abaya area (Chernet, 2011). The letters A to K represent the 12 geothermal sites in the study area. Detailed information about the geothermal sites is shown in Table 1.

**Table 1 List of the geothermal manifestations near the Northern Lake Abaya and their temperature data (Source Geopower Project, 2017)**

Sample	Name	Type	Longitude	Latitude	Altitude (m)	Temp (K)
A	Bilate	Hot Spring	38°02'49.20" E	6°56'31.20"N	-----	-----
B	Dimtu	Well	38°08'02.40"E	6°55'40.80"N	1480	326.95
C	Bilbo Red	Boiling Pool	38°01'51.60"E	6°50'45.60"N	1386	368.55
D	Bilbo 1	Fumarole	38°01'58.80"E	6°50'45.60"N	1392	368.35
E	Tobacco 2	Thermal Spring	38°05'38.40"E	6°49'04.80"N	1355	324.25
F	Tobacco 4	Thermal Spring	38°05'38.40"E	6°49'01.20"N	1355	324.65
G	Tobacco 5	Thermal Spring	38°05'31.20"E	6°48'50.40"N	1348	331.15
H	Tobacco 1	Bubbling Pool	38°05'13.20"E	6°48'39.60"N	1346	336.55
I	Bolosho	Boiling Pool	38°02'42.00"E	6°43'22.80"N	1240	364.65
J	Bolocho	Bubbling Pool	38°02'49.20"E	6°43'19.20"N	1255	338.95

<b>K</b>	Hako	Steam Vent	37°53'52.80"E	6°41'45.60"N	1597	312.75
<b>L</b>	Metincho	Thermal Spring	38°02'06.00"E	6°40'30.00"N	1219	323.45
<b>M</b>	Abaya	Hot Spring	37°53'27.60"E	6°38'45.60"N	-----	-----
<b>N</b>	North Abaya	Thermal Spring	37°55'08.40"E	6°38'45.60"N	1197	313.75
<b>O</b>	North Abaya	Bubbling Pool	37°54'36.00"E	6°38'09.60"N	1200	335.75
<b>P</b>	Maze Well	Well	37°52'08.40"E	6°37'33.60"N	1288	300.35
<b>Q</b>	Boramitta	Bubbling Pool	37°54'07.20"E	6°37'12.00"N	1195	329.55
<b>R</b>	North Abaya	Fumarole	37°54'03.60"E	6°36'54.00"N	1207	364.65
<b>S</b>	North Abaya	Fumarole	37°54'03.60"E	6°36'57.60"N	1207	367.15

### 3. Data sources and materials

ASTER's five bands thermal infrared is the primary remotely sensed data used in the study. It is a medium spatial resolution, 14 bands multispectral imager on the Terra satellite launched in December 1999. It provides TIR images with a 90-m spatial resolution in five channels over 8–12  $\mu\text{m}$  (ASTER user guide, 2003). Thermal bands of the Landsat 7 Enhanced Thematic Mapper Plus (ETM+) and Landsat 8 Operational Land Imager (OLI)/Thermal Infrared (TIRS) are also used, mainly when an ASTER scene of the area was not available.

**Table 2 Specific thermal bands used in the study and their wavelength range**

Sensor	Thermal band	Wavelength range
ASTER	13	10.25 - 10.95
Landsat ETM+	6	10.40 - 12.50
Landsat OLI/TIRS	10	10.60 - 11.19

Thermal infrared (TIR) remote sensing data from Landsat 7 ETM+ (acquired on Feb. 12, 2000, and Jan. 27, 2006); Landsat 8 OLI/TIRS with path 169 and row 055 (obtained on Jan. 25, 2014); and Terra ASTER (received on Mar. 08, 2005; Jan. 01, 2008; Jan. 12, 2012; Dec. 24, 2016; Jan. 28, 2018; and Dec. 01, 2019) have been used for the computation of LST of the study area. The Landsat 7 ETM+ satellite sensor was successfully launched from the Vandenberg Air Force Base on April 15, 1999. Landsat 7 satellite is equipped with ETM+, the successor of Thematic Mapper (TM). The observation bands are essentially the same seven bands as TM, and the newly added panchromatic band 8, with a high resolution of 15-meters was added. Landsat 8 satellite sensor is part of the Landsat Data Continuity Mission and was successfully launched on February 11, 2013. It has two sensors: the OLI and the TIRS. The OLI collects images using nine spectral bands in different wavelengths of visible, near-infrared, and shortwave light to observe a 185 kilometer (115 miles) wide swath of the Earth in 15-30 meters resolution. TIRS bands 10-11: collected at 100 meters but resampled to 30 meters to match OLI multispectral bands. (<https://www.satimagingcorp.com/satellite-sensors/other-satellite-sensors/landsat/>)

MODIS (MOD11A2) Version 6 products, an average of eight days per pixel Land Surface Temperature and Emissivity (LST/E) with a 1 kilometer (km) spatial resolution in 1,200 x 1,200 grids are used to validate the derived LSTs. Availability and less cloud cover of the scene are the criteria to select those dates.

The Landsat images (7 ETM+ and OLI/TIRS) are downloaded from the United States Geological Survey (USGS) (<https://earthexplorer.usgs.gov/>) , whereas AST\_L1T was retrieved from the online Data Pool, courtesy of the NASA Land Processes

Distributed Active Archive Center (LP DAAC), USGS/Earth Resources Observation and Science (EROS) Center, Sioux Falls, South Dakota, using Earth Explorer (<https://search.earthdata.nasa.gov/search>). We use ALOSPALSAR Digital Elevation Model (DEM) (<http://search.asap.alaska.edu>) with a resolution of 12.5 m.

The images together with 1:50,000/1:20,000 scale geological maps of Chericho, Keliso, Tebela and Sodo map sheets from Geological Survey of Ethiopia were used as a base map for mapping geological and hydrothermal manifestation in the study area. Borehole temperature measurements from published data were also used to validate the result of this work. Table 3 shows the summary of the materials used in this study.

**Table 3 List of Geospatial and non-spatial datasets**

Dataset	Sensor	Acquisition Date	Source
Remote sensing Imagery	ASTER L1_T (90m)	08/03/2003 01/01/2008 12/01/2012 24/12/2015 28/01/2018 31/12/2019	<a href="https://search.earthdata.nasa.gov/search">https://search.earthdata.nasa.gov/search</a>
Landsat 7ETM+ (30m)		12/02/2000 27/01/2006	<a href="https://earthexplorer.usgs.gov/">https://earthexplorer.usgs.gov/</a>
Landsat 8 OLI/TIRS (30m)		25/01/2014	
MODIS LST (1km)		2000 (Average of January February and March) 2006 (Average of January February and March) 2014 (Average of January February and March)	<a href="https://earthexplorer.usgs.gov/">https://earthexplorer.usgs.gov/</a>
ALSOPALSAR DEM			<a href="http://search.asap.alaska.edu">https://search.asap.alaska.edu</a>

(12.5m)

Map

Geological Survey of Ethiopia

Geologic Map

(1:50,000)

Hydrothermal

Manifestation Area Map

(1:200000)

Borehole Data

Others	Study area, towns and Woreda shape files	Cer tral Statistical Agency
Band 13 of ASTERs TIR, Band 6 (high gain) of Landsat 7 ETM and Band 10 of Landsat 8 TIRS are selected for this study (Fig 3.). The motivation for the selection is Band 13 provides an excellent statistical fit, with the lowest standard error of estimation ( $\tau=0.5K$ ) and high correlation ( $\gamma=0.98$ ) (e.g., Jimenez, 2007). Band 6 is applicable on LST estimation of Land (non-desert, non-ice) cover type of the Earth (USGS, Landsat7 Handbook). Band 10 is used as Band 11 has a stray light effect (Montanaro et al., 2014) on LST estimation, and it is recommended not to be used by the provider USGS. Moreover, these bands are found in more or less similar wavelength ranges. (Table 2)		

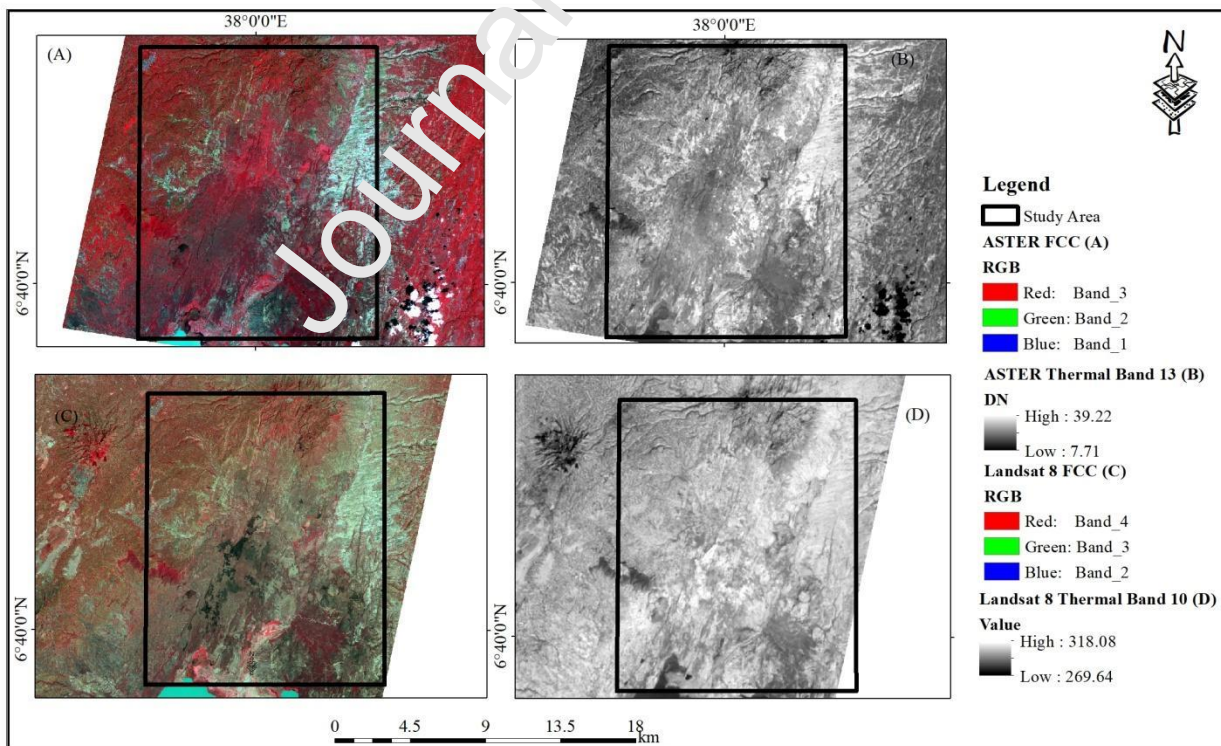


*Figure 3. False-colour composite (FCC) and thermal bands of ASTER (321) (A&B) and Landsat (432) (C&D) respectively of the study area (box).*

#### 4. Method

The study is carried out in five stages (Fig. 4). First, remote sensing data is preprocessed to correct atmospheric and radiometric effects, and geospatial data (geologic maps) are geo-referenced and digitized. In the second stage, the images are processed using emissivity and brightness temperature calculations to determine the LST of the area. MODIS LST products have been used to validate the derived LSTs. The products were multiplied by their scaling factor to get LST values in Kelvin. The fourth stage is geothermal anomaly detection using the preprocessed, medium-resolution satellite imagery. The temperature value next to the mode has been used as the background value for all the nine images. Areas having higher LST values than the background have been considered to be anomalous. Finally, LST values for the last 20 years in 2 years interval is evaluated, and a geothermal anomaly map is produced. The Geothermal sites are dropped on each year LST maps, and their respective values are extracted using the Extract multi values to point tool in ArcGIS.

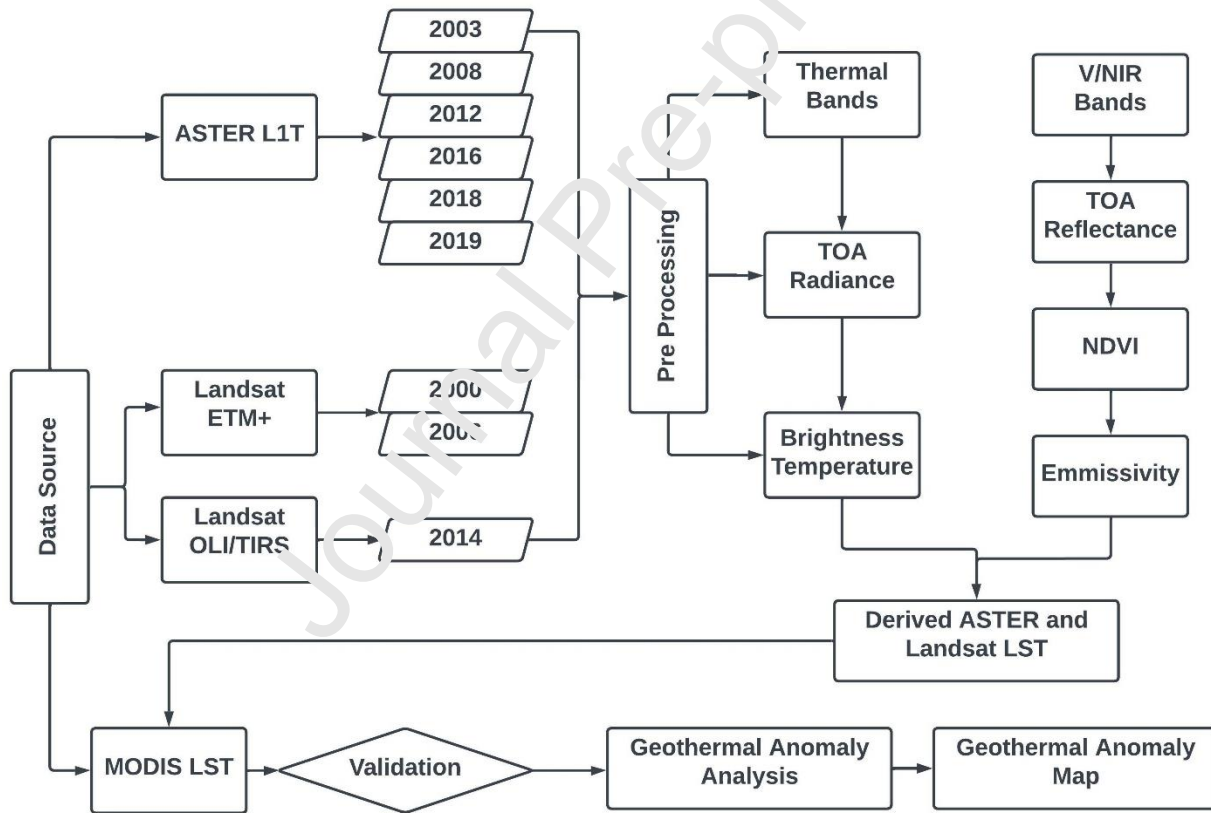


*Figure 4. General flow chart of the method*

##### 4.1 Imagery Preprocessing

Atmospheric correction and radiometric calibration were made for the red, near-infrared and thermal infrared bands of both the Landsat (7ETM+ and 8 TIR) and ASTER images. Dark Object Subtraction (DOS-1) was the algorithm used for conducting the atmospheric correction; it assumes that reflectance from dark objects includes a substantial component of atmospheric scattering. DOS-1 searches each band

for the darkest pixel value. The scattering is removed by subtracting this value from every pixel (Chavez Jr, 1988). QGIS 3.10.1 Semi-Automatic classification plug-in (SCP) has been used for the computation of the algorithm.

#### 4.2 Conversion of Digital Number (DN) to spectral radiance

The at-sensor radiance values at different wavelengths are stored as digital numbers (DN) for convenience during data storage and transfer (ASTER User handbook, 2003). The DN values of the thermal band 13 and visible to near-infrared bands of 2 and 3 for ASTER stored as DN values were converted into spectral radiance values using equation 1. The *UCC* value for each band represents the gain setting used during image acquisition, which can be known from the header file associated with AST\_L1T.

$$L_{rad,x} = UCC_x * (DN_x - 1) \quad (1)$$

Where,

$L_{rad}$  = the spectral radiance of band x,

$UCC_x$  = the unit conversion coefficient of band x.

The DN values of the thermal band 6 of Landsat 7 ETM+ and band 10 of Landsat 8 TIRS and visible to near-infrared bands of 3 and 4 for Landsat 7 ETM+ and 4 and 5 of Landsat 8 OLI data stored as DN values were initially converted to spectral radiance values using equation 2. Constants are provided by USGS from the header file associated with the Landsat product.

$$L_{\lambda} = ML * Qcal + AL \quad (2)$$

Where,

$L_{\lambda}$  = Spectral radiance ( $(W / (m^2 * sr * \mu m))$ );

$ML$  = Radiance multiplicative scaling factor for the band (RADIANCE\_MULT\_BAND\_n from the metadata);

$AL$  = Radiance additive scaling factor for the band (RADIANCE\_ADD\_BAND\_n from the metadata);

$Qcal$  = Level 1 pixel value in DN.

#### 4.3 Emissivity and Land surface temperature calculation

Land Surface Emissivity (LSE) is an important parameter to estimate LST. It is a proportionality factor that scales the black body radiance (Plank's law) to measure emitted radiance, and it is the ability to transmit thermal energy across the surface into the atmosphere (e.g., Jimenez et al., 2006),

In order to retrieve land surface emissivity, we use the approach proposed by Jimenez Munoz et al., 2006 (eq. 3). This approach is based on the following simplified equation

$$\varepsilon = \varepsilon_v + P_v + \varepsilon_s(1 - P_v) \quad (3)$$

Where  $\varepsilon_v$  and  $\varepsilon_s$  are the vegetation and soil emissivity, respectively, and  $P_v$  is the proportion of vegetation.  $P_v$  is calculated using equation 4. A method for calculating  $P_v$  suggests using the NDVI values for vegetation (NDVI\_v) and soil (NDVI\_s) to apply in global conditions (e.g., Sobrino A et al., 2004).

$$P_v = \frac{NDVI - NDVI_s}{(NDVI_v - NDVI_s)^2} \quad (4)$$

#### 4.4 Retrieval of Normalized Difference Vegetation Index (NDVI)

Normalized Difference Vegetation Index (NDVI) is essential to identify different land cover types of a given area. It is calculated using the near-infrared (NIR) and RED bands (Table 6). These bands correspond to band 2 (RED) and 3 N (NIR) for ASTER, band 3 and 4 for Landsat 7 ETM+ and band 4 and 5 for Landsat 8 OLI. This NDVI value is used as an input to calculate emissivity values.

$$NDVI = \frac{\rho_{NIR} - \rho_{RED}}{\rho_{NIR} + \rho_{RED}} \quad (5)$$

Where  $\rho_{NIR}$  is the spectral reflectance of near-infrared band, and  $\rho_{RED}$  is the spectral reflectance of red band.

**Table 4: List of bands used to calculate Normalized Difference Vegetation Index (NDVI)**

Sensor	RED	Near Infrared	Wavelength (nm)	
			RED	NIR
Landsat 7 ETM+	Band 3	Band 4	0.63-0.67	0.77-0.9
Landsat 8 OLI	Band 4	Band 5	0.64-0.67	0.85 - 0.88
ASTER	Band 2	Band 3	0.53-0.69	0.76-0.86

#### 4.5 At-sensor Brightness temperature (BT) estimation

The other step in estimating LST using TIR images is converting spectral radiance to at-sensor Brightness Temperature (BT). The thermal bands are converted from at-sensor spectral radiance to at-sensor brightness temperature; assuming that the Earth's surface is a black body (i.e., spectral emissivity equals 1), and atmospheric effects (absorption and emission along the path) have been taken into account (e.g., Chander *et al.*, 2009). The conversion formula is:

$$BT = \frac{K_2}{\ln(\frac{K_1}{L_\lambda} + 1)} \quad (6)$$

Where BT is at-sensor Brightness Temperature (K),  $L_\lambda$  is corrected at-sensor radiance, and  $K_1$  and  $K_2$  (Table 5) are the pre launch calibration constants (ASTER) and thermal constants (Landsat 7 and Landsat 8) TIR bands.

**Table 5. Calibration and thermal constants of thermal bands**

Sensor	Band	wavelength(nm)	$K_1(W/m^2sr\mu m)$	$K_2(K)$
ASTER	10	8.125-8.475	3047.47	1736.18
	11	8.475-8.825	2480.93	1666.21
	12	8.925-9.275	1930	1584.72
	13	10.25-10.95	866	1350.07
	14	10.95-11.65	649.6	1274.49
Landsat 7ETM+	6	10.40-2.50	666.09	1282.71
Landsat 8 TIRS	10	10.60-11.19	774.89	1321.08
	11	11.50-12.51	480.88	1201.14

The final step is to calculate LST using brightness temperature (BT) of thermal bands and Land Surface Emissivity (LSE) derived from NDVI. LST can be retrieved using equation 7. LST was calculated by applying a structured mathematical algorithm using QGIS 3.10.1 raster calculator tool.

$$T_s = \frac{T_{Sensor}}{1 + (\lambda * \frac{T_{Sensor}}{\rho}) \ln \varepsilon} \quad (7)$$

Where  $T_s$  is the LST in Kelvin (K),  $\lambda$  is the wavelength of emitted radiance (for which the peak response and the average of the limiting wavelength),  $\varepsilon$  is the emissivity calculated in (3), and  $\rho = h \frac{c}{\sigma}$  which is equal to  $1.438 \times 10^{-2}$  mK, where  $\sigma$  is the Boltzmann constant ( $1.38 \times 10^{-23}$  J/K),  $h$  is Planck's constant ( $6.626 \times 10^{-34}$  J s), and  $c$  is the velocity of light ( $2.998 \times 10^8$  m/s) (e.g. Weng et al., 2004). Here we use the above method to estimate the land surface temperature in the Abaya geothermal site at the southern MER.

## 5. Results

### 5.1 Normalized Difference Vegetation Index (NDVI)

The lowest values represented by red colour indicate areas with no vegetation, whereas those appearing green are highly vegetated areas with higher NDVI values. The lowest positive values of the study area are less vegetated soils and barren lands. Water bodies have negative values since water has high absorption and virtually no reflectance near-infrared wavelength ranges and beyond. Vegetated areas, such as forest near and on the elevated regions, croplands near the Lake Abaya and the tobacco plantation, corresponds to higher NDVI values in the study area (see the supplementary file).

The maximum and minimum values of NDVI values (Table 6) for each year have been used to calculate PV, which is the proportion of vegetation and an important factor for calculating emissivity ( $\varepsilon$ ).

**Table 6: NDVI and Brightness Temperature (BT) of Northern Lake Abaya.**

Year	Max NDVI	Min NDVI	S.D. BT	Mean BT	Max BT	Min BT	Max BT ΔT(K)	Min BT ΔT(K)
2000	0.65	-0.69	3.1	310.2	320.6	293.7	-5.0	-3.1
2003	0.89	-0.11	3.6	314.3	325.9	296.5	9.8	4.9
2006	0.57	-0.11	3.0	306.3	316.1	291.9	-4.3	-0.8
2008	0.88	-0.17	3.4	309.2	320.4	292.4	-0.2	-1.3
2012	0.93	-0.23	3.8	307.7	320.5	293.7	-4.7	-0.4
2014	0.53	-0.19	3.0	307.6	321.5	294.6	4.6	1.8
2016	0.89	-0.6	3.4	307.3	320.6	292.3	1.3	14.5
2018	1.00	-0.13	4.4	307.3	319.2	277.8	6.9	-8.2
2019	0.93	-0.19	2.7	301.3	312.3	286	8.5	7.3

### 5.2 Land Surface Emissivity ( $\varepsilon$ )

The emissivity value of the study area is more or less the same throughout the given time frame. It is in the range of 0.99 and 0.96 (see the supplementary file).

### 5.3 Radiometric Temperature

The result of satellite temperature ranges from 278 K to 326 K in the given time frame (Table 6). The highest radiometric temperature (RT) is recorded in the year 2003, having a value close to 326 K. This

could be due to abundant sunlight in the summertime. The lowest value of 312 K is recorded in December 2019. Most of the study area has been covered with vegetation in that particular year.

#### 5.4 Land Surface Temperature

We use the emissivity and radiometric temperature values to generate a land surface temperature map of the study area for each year (see the supplementary file). The LST values range from 283.1 K to 336.2 K. (Table 7) The highest LST values are observed in the NNE, SSW and SE part of the study area. (See the supplementary file) The Northeastern part, which is mainly covered by the lacustrine sediments and pumice deposits, show the highest LST values throughout the given time frame. Highly elevated regions with dense vegetation cover show low LST values.

**Table 7: Derived LST (K) and mode values taken as a background for the Northern Lake Abaya Area**

Year	Max LST	Min LST	Mean LST	SD LST	Mode Value (K)	Background Value (K)
2000	321.6	294.5	311.2	3.2	311	312
2003	336.2	297.2	320.1	5.3	321	322
2006	317.0	292.8	307.0	3.1	307	308
2008	328.6	293.0	313.5	4.6	314	315
2012	327.9	294.6	311.2	5.1	311	312
2014	322.6	295.5	308.6	3.1	308	309
2016	328.0	292.8	311.4	4.3	313	314
2018	323.6	283.1	311.1	4.9	312	313
2019	317.5	290.2	303.1	3.7	301	302

#### 5.5 Validation of Land Surface Temperature Anomalies

The LST of a given area can be retrieved from different TIR sensors and compared on spatial scales if their overpass time is close to the satellite being used. We use MODIS LST Product data to validate the derived LST values. Both the derived LSTs and the MODIS LST product are re-sampled to 100m Dusing ArcGIS 10.4.1(ESRI, 2016) resampling tool.

#### 5.6 Geothermal Anomaly detection Using Remote Sensing

Previous studies consider the mode LST values as background and hence LST values higher than this value considered as anomalous (e.g., Qin et al., 2011; Darge et al., 2019). We follow a similar approach. Minimum-Maximum stretch type symbology in ArcMap10.4.1 has been used to highlight and map areas with the highest LST values (open circle). Urban areas tend to have greater emitted radiance recorded by a sensor. These might be regarded as geothermal potential anomalous areas during interpretation and mislead the analyst. Therefore, a 1000m buffer from urban areas has been created and excluded from the geothermal anomaly maps to reduce the urban effect.

The mode value for the year 2000 was 311 K. Around thirteen areas having LST values 3 to 7 K more significant than the background value has been traced in the northeastern and southwestern part of the study area (Fig 5). For the year 2003, the mode value was 321 K, fifteen places with LST values 4 to 11 K higher than the background has been identified. The northeastern and southwestern part of the study area shows the highest LST values close to 330K. The Bolocho Vasca bubbling pool and the North Abaya thermal Springs were identified to be anomalous in the year 2000 while the Dimtu well, Bilbo1 fumaroles, Bilbo red bubbling pool, Metincho thermal spring and Maze well are among the identified anomalous areas with geothermal potential in both years. (See the supplementary file).

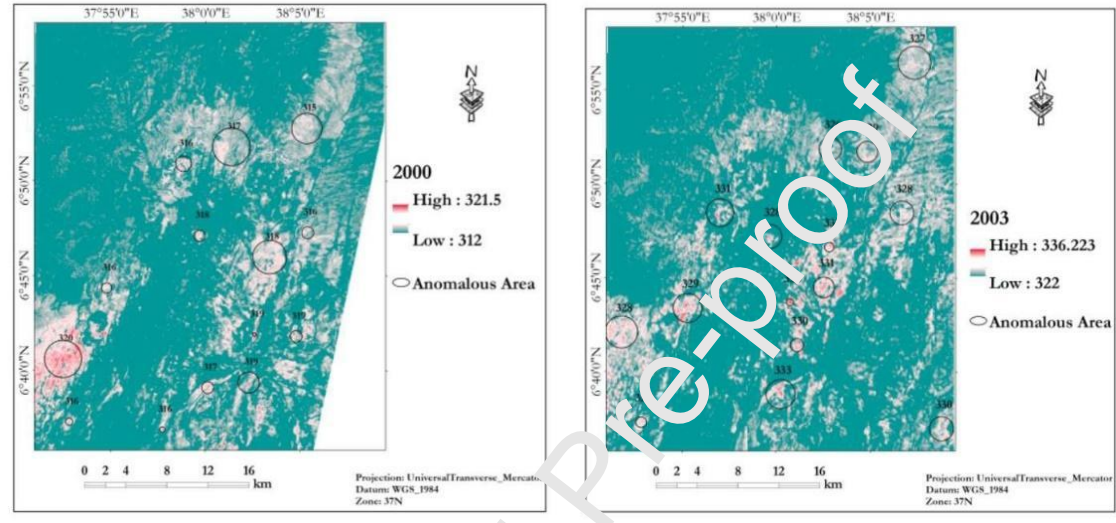
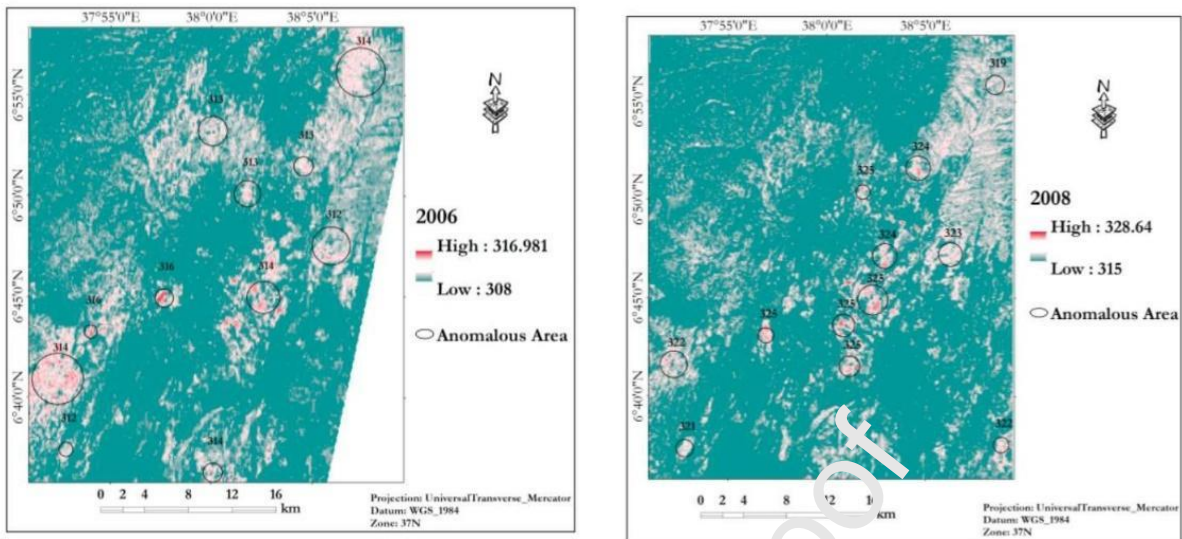


Figure 5. Identified anomalous areas for the year 2000 and 2003

For the year 2006, the mode value was 207 K; areas having LST values of 4 to 8 K greater than the background has been identified in the North eastern, central, and south western parts of the study area which is mainly covered with the Abela fissural basalt (Qb1), lacustrine sediment (Q11/Qp1), and recent basalt flows and scoria cones ('O<sub>1</sub>'') (Fig 2). On the other hand, the mode value for the year 2008 was 314 K, more than ten areas having 4 to 12 K LST values greater than the background have been identified. The Dimtu well, Bilbo 1 Fumaroles, Bilbo Red boiling pool were traced to be anomalous in both years, while the Bolocho Vasca bubbling pool, the thermal springs near the Tobacco plantation and Metincho area are among the identified area with the highest LST values in the year 2008 (Fig 6).



*Figure 6. Identified anomalous areas for the year 2006 and 2008*

In the year 2012, the mode value was 311 K; areas with greater LST values had been traced on the NNE and NE part of the study area. The Anka Bilbo fumaroles and bubbling pools together with the Dimtu well have been identified as anomalous areas once again. In addition, the Tobacco 2 thermal spring and the Bolosho vasca bubbling pools have also been determined to be anomalous in the year 2012. For 2014, the mode value was 308 K. Areas with the highest LST values had been traced in the southwestern part of the study area (Fig 7). The Bolosho Vasca and Bijo red boiling pool, Tobacco 1 bubbling pool, and the Maze well are among the identified anomalous areas (Supplementary file).

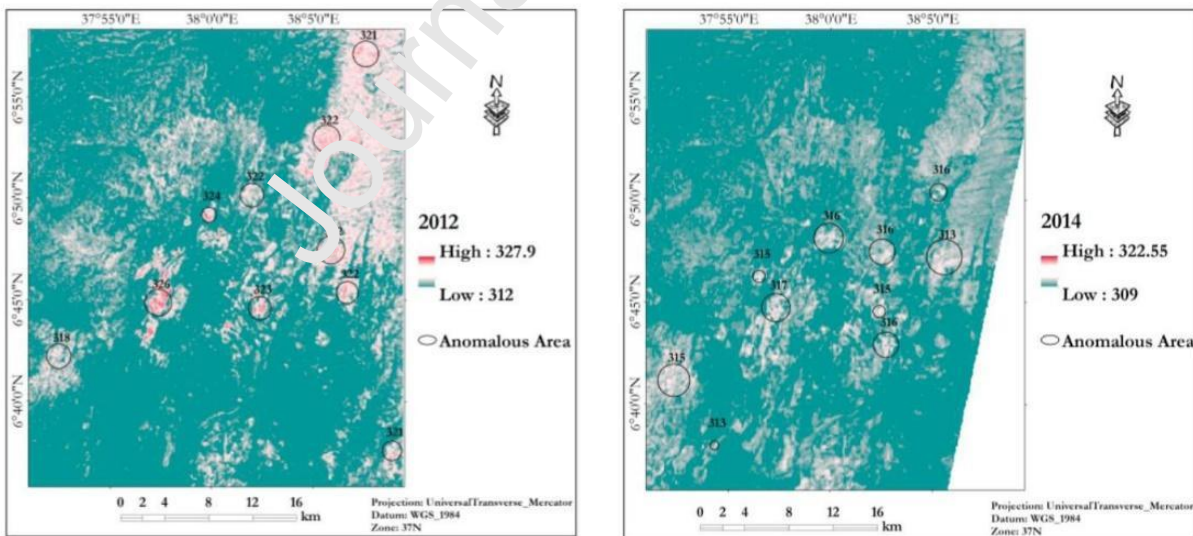


*Figure 7. Identified anomalous areas for the year 2012 and 2014*

The mode LST values were 313,312 and 301 K for 2016, 2018 and 2019, respectively. Around ten areas with LST values 4 to 14 K higher than the background have been identified in the year 2016. Areas

found in the southern part of the study area show the highest LST values greater than 320K. The Bolocho Vasca bubbling pool, the Bilbo 1 fumaroles, the Dimtu well and the Bilbo red boiling pools are among the identified anomalous areas (Fig 8). For the year 2018, the NNE and central part of the study area shows the highest LST values. In 2019, around 15 areas with LST values 8 to 15 K higher than the background had been identified (Fig 9), including the Dimtu well, the thermal springs near the tobacco 4 and metincho, Bolocho vasca, and Tobacco 1 bubbling pool, the Northern Abaya fumaroles (7,9) and spring, the Anka Bilbo fumaroles and red boiling pool, the Tobacco 2 and 5 thermal springs together with the Bolosho 2 boiling pool. (The Last five were also anomalous in the year 2018).

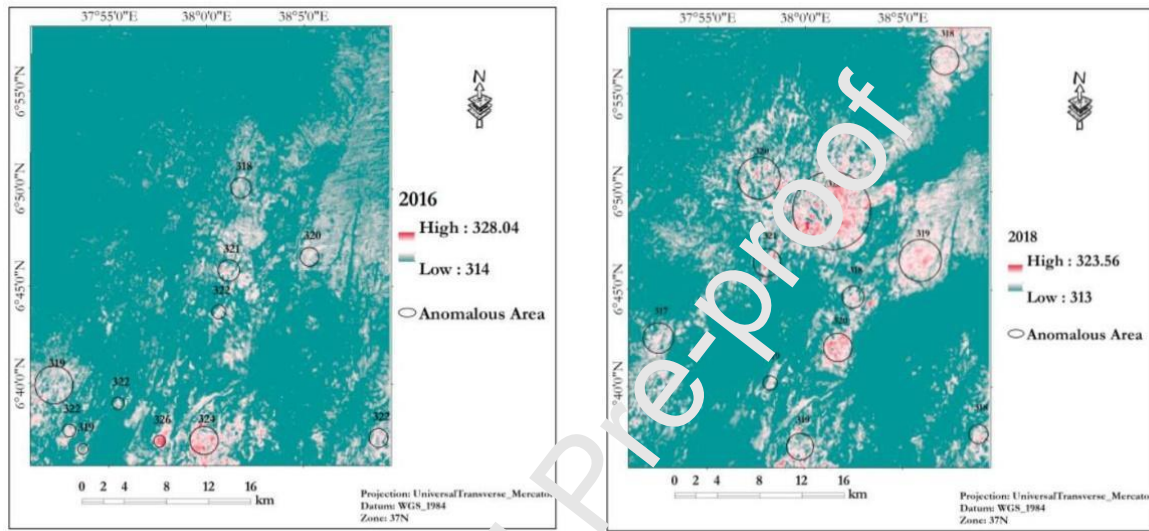


*Figure 8. Identified anomalous areas for the year 2016 and 2018*

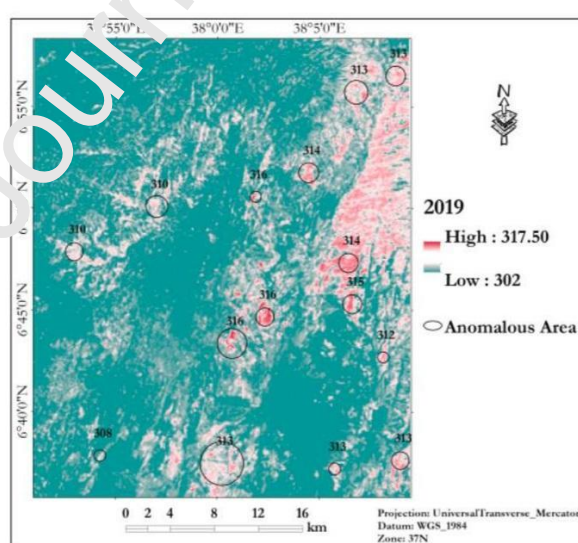


*Figure 9. Identified anomalous areas for the year 2019*

The Anka Bilbo boiling pools and fumaroles, the Dimtu well and Bolocho Vasca bubbling pools appear to be anomalous more than five times. The Maze well, and tobacco 1 bubbling pools were analyzed to be anomalous four times. Metincho and Tobacco 2 thermal springs appear to be anomalous two times out of nine. (Table 8) The Abaya hot spring, Bilate hot springs, the Hako steam vent and Boramitta bubbling pools are among the known surface manifestations that happened to be anomalous in none of the years in the given time frame (2000-2019 in two years intervals). Volcano sedimentary rocks, Pleistocene basalt, pumice, unwelded tuff, rhyolitic and trachytic lava flows are the major lithological units associated with higher surface temperature values. Nineteen known anomalous areas from the geological Survey and previous literatures have been collected as a sample for the validation against the derived LSTs (See the supplementary file).

**Table 8 List of the Northern Abaya Surface Heat Manifestation and particular years they appear to be Anomalous. The 1 and 0 values indicate the anomaly in specific year fits and doesn't fit with the surface heat manifestation, respectively.**

Name	2000	2003	2006	2008	2012	2014	2016	2018	2019
Abaya	0	0	0	0	0	0	0	0	0
Biilate	0	0	0	0	0	0	0	0	0
Bilbo 1	1	1	1	1	1	0	1	1	1
Bilbo Red boiling pool	1	1	1	1	1	1	1	1	1
Bolocho vasca	1	1	0	1	1	1	1	0	1
Bolosho 2	0	0	0	0	0	0	0	1	1
Boramitta	0	0	0	0	0	0	0	0	0
Dimtu Well	1	1	1	1	1	0	0	0	1
Hako	0	0	0	0	0	0	0	0	0
Maze well	1	1	1	0	0	1	0	0	0
Metincho	1	1	0	1	0	0	0	0	0
North Abaya	1	0	0	0	0	0	0	0	1
N.Abaya Fumarolic Field 7	0	0	0	0	0	0	0	0	1
N. Abaya Fumarolic Field 9	0	0	0	0	0	0	0	0	1
North Abaya Spring	1	0	0	0	0	0	0	0	0
Tobacco 1	1	0	0	1	0	1	0	0	1
Tobacco 2	0	0	0	0	1	0	0	1	1
Tobacco 4	0	0	0	0	0	0	0	0	1
Tobacco 5	0	0	0	0	0	0	0	1	1

## 6. Discussion

### 6.1 Surface Temperature changes of the surface manifestations near Lake Abaya.

Monitoring of fumaroles activity at Aluto volcano using ASTER night time imageries show a temperature change of 1 to 9°C over a given time (2004-2006) (e.g., Braddok et al., 2017). Our study in the Abaya geothermal area indicates an average temperature change of 7.6 K between 2000 and 2020. The maximum temperature change of 14.7K is attained in the Maze well, whereas the lowest temperature change of 1.8K is attained in the thermal springs near the tobacco 4. Table 10 presents the surface temperature changes of the surface heat manifestations near the Lake Abaya area. Places like Abaya, Bilate, Boramita and Hako have low LSTs in almost all the 9 images and could not be determined as a geothermal area using the method applied even if they were identified to be anomalous by different researches (e.g. Cherenet, 2011; Kebede, 2015). Other places like North Abaya, Bolosho 2 have low

LSTs in about 7 images (Table 8); this shows that using a single satellite image to show geothermal anomaly is not enough like in many researches (e.g., Darge et al., 2019). The spatial resolution of the sensor, the acquisition date of satellite images being used, the size and type of the surface manifestations and the land covers of their surrounding are among the factors that influence the detectability of anomalous areas and the surface heat manifestations near Lake Abaya area.

## 6.2 Time versus LST values

Analysis of LST with time (Table 9) shows that LST of the geothermal sites in the northern lake Abaya prospect area did not vary that much within the 20 years that the analysis has been made. The correlation ( $R^2$  value between 0.07 and 0.53) between time and the derived LSTs shows an inverse relationship in most of the sites. In some cases, no correlation at all. This indicates that there shouldn't be any considerable LST change in anomalous geothermal areas and confirms that the satellite results are correct (see supplementary file).

**Table 9 List of the known hydrothermal manifestations in the Northern Lake Abaya area**

Name	Type	$R^2$
Dimtu	Well	0.29
Bilbo 1	Fumaroles	0.09
Bilbo Red	Boiling pool	0.07
Tobacco 1	Bubbling pool	0.34
Tobacco 2	Thermal spring	0.06
Tobacco 4	Thermal spring	0.03
Tobacco 5	Thermal spring	0.04
Bolosho Vasca	Bubbling pool	0.22
Bolosho 2	Boiling pool	0.28
Metincho	Thermal 1 spring	0.13
Abaya	Hot spring	0.12
Bilate	Hot spring	0.19
North Abaya	Bubbling pool	0.17
North Abaya Spring	Thermal Spring	0.35
Maze Well	Well	0.40
North Abaya Fumaroles (7)	Fumaroles	0.40
North Abaya Fumaroles (9)	Fumaroles	0.40
Hako	Steam Vent	0.40
Boramitta	Bubbling pool	0.53

## 6.3 Comparison of the derived LSTs with the borehole data.

Borehole data of the geothermal sites in the northern Lake Abaya area (Table 10) from the Geological Survey of Ethiopia (GSE) and other literature (e.g. Chernet, 2011) have been compared with the average derived LSTs. The result shows that the difference is in the range of 1.5 to 55.9K. A temperature difference of less than 25K has been traced in 10 sites out of 15. The North Abaya spring, Metincho and tobacco 2 thermal springs are among the sites with the lowest temperature difference. The average LST value of the Northern Abaya spring, Metincho and Tobacco 2 thermal spring is 312.3, 323.5 and 324.3K with a temperature difference of 1.5, 10.4, and 10.5K, respectively, from the borehole data. (Table 10)

**Table 10 Derived LSTs (2000-2019) Versus Temperature measurements of a borehole data**

Name	2000	2003	2006	2008	2012	2014	2016	2018	2019	T(K)	Average T°(K)	Difference(K)
Bilbo 1	314.48	327.58	311.22	323.17	320.07	310.54	319.04	319.83	308.09	368.4	317.1	51.2
Bilbo Red	314.74	329.20	311.72	324.19	318.51	311.35	320.65	320.58	310.63	368.6	318.0	50.6
Bolocho vasca	314.00	331.69	309.43	321.75	315.73	312.57	317.68	313.43	305.66	339.0	315.8	23.2
Bolosho 2	312.71	319.08	305.98	310.75	306.15	308.92	314.95	315.94	306.54	364.7	311.0	53.6
Dimtu Well	314.74	330.28	310.96	322.34	319.57	310.06	315.07	313.36	306.04	327.0	315.8	11.1
Maze well	317.94	324.86	310.96	311.69	303.78	312.59	312.24	311.3	303.19	300.4	312.0	11.6
Metincho	314.49	325.12	303.05	317.49	312.88	309.22	313.48	314.98	305.98	323.5	313.0	10.5
North Abaya	310.94	319.97	308.37	315.8	310.81	309.71	314.30	312.91	303.23	335.8	311.8	24.0
North Abaya Fumarolic Field 7	312.99	319.38	308.63	312.08	307.09	309.1	311.98	308.6	305.26	364.7	310.6	54.1
North Abaya Fumarolic Field 9	312.99	321.51	308.63	313.71	307.95	309.17	312.63	308.13	306.12	367.2	311.2	55.9
North Abaya Spring	314.49	321.87	309.67	315.18	308.01	310.59	314.96	311.34	304.48	313.8	312.3	01.5
Tobacco 1	314.98	319.88	308.89	315.98	311.26	310.99	311.15	314.42	304.97	336.6	312.6	23.9
Tobacco 2	311.71	322.62	308.9	316.65	315.88	309.69	314.77	317.03	307.84	324.3	313.9	10.4
Tobacco 4	309.14	318.98	306.53	313.27	312.52	309.11	311.11	314.04	307.34	324.7	311.3	13.3
Tobacco 5	309.16	321.00	307.08	311.14	312.29	307.93	312.99	315.35	305.28	331.2	311.4	19.8

The spatial resolution of the satellite compared to the field data gives rise to a temperature difference of such attained value. The temperature values of the field data are much closer to the LST values of the year 2003. The derived LSTs are estimated using a sensor 90m above the ground, which is a very small resolution compared to a field survey. Moreover, borehole data records subsurface temperature, unlike the satellites that are sensitive to surface temperatures. A further investigation is needed to determine the exact locations of previously mapped geothermal sites so that a temperature from the subsurface and the surface could be compared. A remote sensing and Earth observation tools can be used to easily understand and figure out areas with geothermal potential quickly, and to investigate the subsurface environment. Our study improves exploration strategies in regions where direct exploration may not always be feasible.

## Conclusion

We used the single-channel algorithm to derive land surface temperature (LST) for the Abaya geothermal area in the Main Ethiopian Rift and compared our results with the available borehole temperature measurements. Our combined analysis shows that one-time image analysis may not be suitable to properly identify geothermal anomaly sites and multi-temporal image analysis gives a better result as it helps to identify time-series anomalies.

The temperature value next to the mode has been used as the background value for all the nine images. Areas having higher LST values than the background have been considered to be anomalous. Areas with temperature values as high as 333K have been measured in the year 2003. The mean LST is highest in 2003 (320.1 K) and lowest in 2019 (303.1 K). The change in mean LST was between -9 K to 13 K. These LST results from ASTER images were validated with MODIS LST products and show more than 0.6 correlations.

We compared the derived LSTs from the nine images with the borehole temperature data. The LSTs at the year 2003 have been much closer to the temperature value from borehole data (Sub-surface temperature). However, the main limitation here is that the borehole measurements lack information about the depth at which temperature is taken, which has a series consequence especially if the measurements are taken at shallower depth. Nevertheless, we argue that our results are quite reasonable. Furthermore, the geothermal anomaly areas were validated with the existed field data (19 sites), out of which 15 sites (79%) fall in the identified geothermal anomaly areas.

The correlation between time and LST values in known geothermal activity sites shows no correlation (less than 0.5) except one site, Boramitta (0.53). This indicates that even though LST varies with time (e.g., day and night and seasonal changes), the LST of areas with geothermal potential remain more or less constant on yearly basis. The results also indicate that thermal infrared remote sensing is an effective method for geothermal exploration, especially for the pre visibility of geothermal exploration. The methodology applied in this work has efficiently reduced the extent for geothermal exploration and locate the promising geothermal areas for further investigation. However, it can only detect the surficial thermal anomaly and is sensitive to the geothermal resource covered by vegetation/forest with small in size. Therefore, geologic analysis and the mechanism of the geothermal anomaly are required to assist and facilitate the identification of geothermal areas with TIR remote sensing. With the knowledge of geothermal mechanisms and the complement from the geological investigation, the accuracy of geothermal detection using TIR remote sensing could be significantly enhanced.

**Acknowledgment:** BTH, AAM, and TK acknowledge the support from USAID-NAS GEOPOWER Africa Project. AAM is supported by the Alexander von Humboldt foundation (Georg Forster fellowship for experienced researchers at GFZ Potsdam.)

**Author Contributions:** TT data collection and analysis, writing of the first draft and figure preparation. BTH - data analysis and interpretation, supervision and writing of the final draft; AAM interpretation of results and writing of the final draft; TK- writing of the final manuscript.

**Conflicts of Interest:** The authors declare no conflict of interest.

Journal Pre-proof

## Reference List

1. Abiye, T.A., 2003. 'Controls on the occurrence of cold and thermal springs in the central Ethiopia'. *African Geoscience Review*. 19(4):245-251
2. ASTER Reference guide version 1 (2003) ERSDAC Earth Remote Sensing Data Analysis Center. <http://www.science.aster.ersdac.or.jp/en/index.html>
3. Agostini, A., Bonini, M., Corti, G., Sani, F., and Manetti, P. (2011). 'Distribution of Quaternary deformation in the central Main Ethiopian Rift, East Africa'. *Tectonics* 30:TC4010. doi: 10.1029/2010TC002833
4. Ayele , A., Teklemariam, M., Kebede, S., 2002. 'Geothermal Resource Exploration in the Abaya and Tulu Moye-gedemsa Geothermal prospects, Main Ethiopian Rift. Technical Report.' Geological Survey of Ethiopia, Addis Ababa, Ethiopia.
5. Braddock, M., Biggs, J., Watson, I.M., Hutchison, W., Pyle, D M., Mather, T.A., 2017. 'Satellite observations of fumaroles activity at Aluto volcano, Ethiopia: Implications for geothermal monitoring and volcanic 'hazard', *Journal of Volcanology and Geothermal Research* (doi: 10.1016/j.jvolgeores
6. Calvin, W. M., Littlefield, E. F., and Kratt, C., 2015. 'Remote Sensing of geothermal-related resource exploration in Nevada'. *Geothermics*. 53,517-526. <https://doi.org/10.1016/j.geothermics.2014.09.002>
7. Chan, H., Chang, C. and Dao, P., 2018. 'Geothermal Anomaly Mapping Using Landsat ETM+ Data in Ilan Plain, Northeastern Taiwan.' *Pure and Applied Geophysics*. 175: 303-323.
8. Chander, G., Markham, B. L., Helder, D ., 2009. 'Summary of current radiometric calibration coefficients for Landsat MSS, TM, ETM+, and EO-1 ALI 'sensors'. *Remote Sensing of Environment*, 113(5): 893-903. <http://doi.org/10.1016/j.rse.2009.01.007>
9. Chernet T., (2011). Geology and hydrothermal resources in the northern Lake Abaya area, Ethiopia. *Journal of African Earth Sciences*, 61: 129-141.
10. Coolbaugh, M.F., Kratt, C., Fahacaro, A., Calvin, W.M., Taranik, J.V., 2007. 'Detecting of geothermal anomalies using Advanced Thermal Emission and Reflection Radiometer (ASTER) thermal infrared images at Brady's Hot springs, Nevada, 'USA'. *Remote Sensing of Environment* 106(3):350-359.
11. Corti, G., Sani, F., Floris, A.A., Greenfield, T., Keir, D., Erbello, A., Muluneh, A.A., Ayele, A., 2020. 'Tectonics of the Asela-Langano Margin, Main Ethiopian Rift (East Africa)'. *Tectonics*, 39(8). <https://doi.org/10.1029/2020TC006075>.
12. Dar, I., Qadir, J., Shukla, A., 2019. 'Estimation of LST from multisensor thermal remote sensing data and evaluating the influence of sensor 'characteristics', *Annals of GIS*, 25:3, 263-281, DOI: 10.1080/19475683.2019.1623318
13. Darge, Y.M., Hailu, B.T., Muluneh, A.A., Kidane T., 2019. 'Detection of geothermal anomalies using Landsat 8 TIRS data in Tulu Moye geothermal prospect, Main Ethiopian 'Rift'. *Applied Earth Observation Geoinformation*. 74: 16-26.
14. Eneva, M., Coolbough, M., Combs, J., 2006. 'Application of Satellite thermal infrared imagery to geothermal exploration in east central 'California'. *Transactions - Geothermal Resources Council*.30:407-411.
15. ESRI, 2016. Using Arc Map 10.4. <https://desktop.arcgis.com/en/arcmap/10.4/tools/data-management-toolbox/resample.htm> (Accessed Jun. 18 2021).

16. Greenfield, T., Keir, D., Kendall, J.-M., Ayele, A., 2020. ' Seismicity of the Bora-Tullu Moye Volcanic Field,2013-2017 '. *Earth and Planetary Science Letters*. 526 – 115782.
17. Haselwimmer, C., Prakash, A., and Holdmann, G., 2013. 'Quantifying the heat flux and outflow rate of hot springs using airborne thermal imagery: Case study from Pilgrim Hot springs, 'Alaska'. *Remote Sensing of Environment*. 136:37-46. <https://doi.org/10.1016/j.rse.2013.04.008>
18. <https://www.satimagingcorp.com/satellite-sensors/other-satellite-sensors/landsat/>) accessed on March,03, 2022.
19. Jimenez-Munoz, J.C., Sobrino, J.A, 2007. 'Feasibility of Retrieving Land-Surface Temperature From ASTER TIR Bands using Two-Channel Algorithms, A case study of Agricultural 'Areas'. *IEEE Geoscience and Remote Sensing Letters*, 4 (1)
20. Jimenez-Munoz, J.C., Sobrino, J.A., Gillespie A., Sabol, D., Gustafson, W.T., 2006. 'Improved land surface emissivity over agricultural areas using ASTER 'NDVI'. *Remote Sensing of Environment*, 103: 474-487.
21. Kebede S., (2015) 'Country update on geothermal exploration and development in 'Ethiopia'. In: Presented at Short Course IX on Exploration for Geothermal resources, organized by UNU-GTP, GDC and KenGen, at Lake Bogoria and Lake Naivasha, Kenya, Nov. 9 - Dec.1
22. Keir, D., Ebinger, C.J., Stuart, G.W., Daly, E., Ayele, a., 2006. 'Strain accommodation by Magmatism and faulting as rifting proceeds to breakup: Seismicity of the northern Ethiopian 'rift'. *Journal of Geophysical Research: Solid Earth*. 111(B5). <https://doi.org/10.1029/2005JB003748>.
23. Chavez Jr, P.S. (1988). 'An improved da.<sup>1</sup>-of object subtraction technique for atmospheric scattering correction for multispectral data'. *Remote Sensing of Environment*, 24: 459-479
24. Lapins, S., Kendall, J.-M., Ayele, A., Vil's, M., Nowacki, A., Cashman, K., 2020. 'Lower-Crustal Seismicity on the Eastern Border Faults of the Main Ethiopian Rift '. *J. Geophys. Res.* 125-8. <https://doi.org/10.1029/2020JB020057>
25. Minissale, A., Cortia, G., Tassan, F., Darrah, T.H., Vaselli, O., Montanari, D., Montegrossi, G., Yirgu, G., Selmo, E., Teclu, A., 2017. 'Geothermal potential and origin of natural thermal fluids in the northern Lake Abaya area, Main Ethiopian Rift, East Africa." *J. Volcanol. Geoth. Res.* 336, 1–18. <https://dx.doi.org/10.1016/j.volgeores.2017.01.012>
26. Muluneh, A. A., Cuffaro, M., Kidane, T., 2017. 'Along- strike variation in deformation style inferred from kinematic reconstruction and strain rate analysis: A case study of the Ethiopian Rift'. *Physics of the Earth and Planetary Interiors*, 270:176-182. <https://doi.org/10.1016/j.pepi.2017.07.009>
27. Muluneh, A. A., Keir, D., Corti, G., 2021. 'Thermo-Rheological Properties of the Ethiopian Lithosphere and Evidence for Transient Fluid Induced Lower Crustal Seismicity Beneath the Ethiopian Rift.' *Front. Earthsci.*, <https://doi.org/10.3389/feart.2021.610165>
28. Muluneh, A.A., Cuffaro, M., Doglioni, C., 2014. 'Left- lateral transtension along the Ethiopian Rift and constraints on the mantle-reference plate 'motions' *Tectonophysics*: 632, 21-31.
29. Ogden, C.S., Keir, D., Bastow, I.D., Ayele, A., Marcou, S., Ugo, F., Woodward, A., Kibret, B.A., Gudbrandsson, S., 2021. 'Seismicity and Crustal Structure of the Southern Main Ethiopian Rift:New Evidence from Lake Abaya'. *Geochemistry, Geophysics, Geosystems*. Vol 22-8. <https://doi.org/10.1029/2021GC009831>
30. Omenda, P.A., and Teklemariam, M., 2010. 'Overview of geothermal resource utilization in the east African rift 'system'. In: *Presented at Short Course V on Exploration for Geothermal*

*Resources*, organized by UNU-GTP, GDC and KenGen, at Lake Bogoria and Lake Naivasha, Kenya, Oct. 29 – Nov. 19.

31. Purschel, M., Gloaguen, R., Stadler, S., 2013. "Geothermal activities in the Main Ethiopian Rift: hydro geochemical characterization of geothermal waters and geothermometry applications (Dofan-Fantale, Gergede-Sodere, Aluto-Langano)." *Geothermics* 47: 1–12.
32. Qin, Q., Ning, Z., Peng, N., Leile, C., 2011. 'Geothermal area detection using Landsat ETM+ thermal infrared data and its mechanistic analysis—A case study in Tengchong, China." *Int. J. Appl. Earth Obs. Geoinformation* 13, 552–559.
33. Reinsch, T., Dobson, P., Asanuma, H., Huenges, E., Poletto, F., Sanjuan, B., (2017). "Utilizing supercritical geothermal systems: a review of past ventures and ongoing research activities". *Geothermal Energy* 5:16. <https://doi.org/10.1186/s40517-017-0075-y>
34. Siegburg, M., Bull, J.M., Nixon, C.W., Keir, D., Gernon, T.M., Corti, G., Abebe, B., Sanderson, D.J., Ayele, A., 2020. 'Quantitative Constraints on Faulting and Fault slip Rates in the Northern Main Ethiopian Rift.' *Tectonics*: 39(8), DOI.org 10.1029/2019TC006046
35. Sobrino, J.A., Jimenez-Munoz, J.C, Paolini, L., 2004. 'Land surface temperature retrieval from LANDSAT TM 5.' *Remote Sensing of Environment* 90(1):454-4430
36. Teklemariam, M., 2008. 'Strategic plan for geothermal exploration and development in 'Ethiopia'. In: Presented at Short Course III on Exploration for Geothermal Resources, organized by UNU-GTP and KenGen, at Lake Naivasha, Kenya, Oct. 24 – Nov. 17.
37. USGS, 1998. 'Landsat 7 Science data user's handbook'. <https://doi.org/10.3133/7000070>. (Accessed on Jun. 10 2020)
38. Montanaro, M., Gerace, A., Lunsford, A., Reuter, D., 2014. 'Stray Light Artifacts in Imagery from the Landsat 8 Thermal Infrared Sensor.' *Remote Sens.* 11:10435-10456; <https://doi:10.3390/rs61110435>
39. Van der Meer, F., Hecker, C., Van Ruitenbeek, F., Van der Werff, H., de Wijkerslooth, C., Wechsler, C., 2014. 'Geological remote sensing for geothermal exploration': a review *Int. J. Appl. Earth Obs. Geoinformation* 33: 255–269.
40. Vaughan, R. G., Keszthelyi, I. P., Lowenstein, J. B., Jaworowski, C., and Heasler, H., 2012. 'Use of ASTER and MODIS thermal infrared data to quantify heat flow and hydrothermal change at Yellowstone National Park'. *Journal of Volcanology and Geothermal Research*.233-234:72-89. <https://doi.org/10.1016/j.jvolgeores.2012.04.022>
41. Wang, K., Giang, O , Yu, D., Yang, Q., Wang, L., Han, T.C., Xu, X., 2019. 'Detecting daytime and nighttime land surface temperature anomalies using thermal infrared remote sensing in Dandong geothermal 'prospect'. *International Journal of Applied Earth Observation and Geoinformation*. 80:196-205
42. Weng, Q., Lu, D., Schubring, J., 2004. 'Estimation of land surface temperature–vegetation abundance relationship for urban heat island 'studies'. *Remote Sensing of Environment* 89 (4), 467–483.

**Authors Statement**

Binyam Tesfaw Hailu, Ameha Atnafu Muluneh, and Tesfaye Kidane acknowledge the support from USAID-NAS Geopower Africa Project. Ameha is supported by the Alexander von Humboldt foundation (Georg Forster fellowship for experienced researchers at GFZ Potsdam.).

The Authors Contributions: Tsion Taye contributed on the data collection and analysis, writing of the first draft and figure preparation. Binyam Tesfaw Hailu contributes on idea investigation, data analysis and interpretation, supervision and writing of the final draft. Ameha Atnafu Muluneh interpretation of results and writing of the final draft. Tesfaye Kidane - supporting the geoscience concept, scientific paper writing and reviewing of the final manuscript.

Journal Pre-proof

**CONFLICT OF INTEREST STATEMENT**

**Manuscript title:**

DETECTION OF GEOTHERMAL ANOMALIES IN THE NORTHERN LAKE ABAYA  
GEOTHERMAL FIELD, MAIN ETHIOPIAN RIFT

**Conflict of Interest:**

*The authors declare no conflict of interest.*

Journal Pre-proof

## **Highlights**

- This research aims to identify geothermal anomaly areas in the geologically active region of the southern Main Ethiopian Rift.
- Multi-temporal TIR data from 2000 through 2019 from Landsat 7 and 8 TIR instruments ASTER data and field-based temperature data from 19 sites were used for the analysis.
- The mean LST is highest in 2003 (320.1 K) and lowest in 2019 (303.1 K).
- LST of ASTER images showed a correlation coefficient greater than 0.6 with MODIS LST products.
- Fifteen sites (79 % of the observed data) fit with the identified geothermal anomaly areas.